2018

High-Frequency Thermal-Fluidic Characterization of Dynamic Microchannel Flow Boiling Instabilities: Part 2 - Impact of Operating Conditions on Instability Type and Severity

T. A. Kingston

J. A. Weibel
Purdue University, jaweibel@purdue.edu

S V. Garimella
Purdue University, sureshg@purdue.edu

Follow this and additional works at: https://docs.lib.purdue.edu/coolingpubs

Kingston, T. A.; Weibel, J. A.; and Garimella, S V., "High-Frequency Thermal-Fluidic Characterization of Dynamic Microchannel Flow Boiling Instabilities: Part 2 - Impact of Operating Conditions on Instability Type and Severity" (2018). *CTRC Research Publications*. Paper 331.
http://dx.doi.org/https://doi.org/10.1016/j.ijmultiphaseflow.2018.05.001

High-Frequency Thermal-Fluidic Characterization of Dynamic Microchannel Flow Boiling Instabilities: Part 2 – Impact of Operating Conditions on Instability Type and Severity[1]

Todd A. Kingston, Justin A. Weibel, and Suresh V. Garimella[*]

Cooling Technologies Research Center

School of Mechanical Engineering, Purdue University, West Lafayette, Indiana 47907 USA

Abstract

Dynamic instabilities during flow boiling in a uniformly heated microchannel are investigated. The focus of this Part 2 of the study is on the effect of operating conditions on the instability type and the resulting time-periodic hydrodynamic and thermal oscillations, which have been established after the initial boiling incipience event. Part 1 of this study investigated the rapid-bubble-growth instability at the onset of boiling in the same experimental facility. Fluid is driven through the single 500 μm-diameter glass microchannel by maintaining a constant pressure difference between a pressurized upstream reservoir and a reservoir downstream that is open to the ambient, so as to resemble the hydrodynamic boundary conditions of an individual channel in a parallel-channel heat sink. Simultaneous high-frequency measurement of pressure drop, mass flux, and wall temperature is synchronized to high-speed flow visualizations enabling transient characterization of the thermal-fluidic behavior. The effect of flow inertia, inlet liquid subcooling, and heat flux on the hydrodynamic and thermal oscillations and time-averaged

---

[*] Corresponding author
E-mail addresses: kingston@purdue.edu (T.A. Kingston), jaweibel@purdue.edu (J.A. Weibel), sureshg@purdue.edu (S.V. Garimella)

performance is assessed. Two predominant dynamic instabilities are observed: a time-periodic series of rapid-bubble-growth instabilities, and the pressure drop instability. A spectral analysis of the time-periodic data is performed to determine the characteristic oscillation frequencies. The heat flux, ratio of flow inertia to upstream compressibility, and degree of inlet liquid subcooling significantly affect the thermal-fluidic characteristics. High inlet liquid subcoolings and low heat fluxes result in time-periodic transitions between single-phase flow and flow boiling that cause large-amplitude wall temperature oscillations due to a time-periodic series of rapid-bubble-growth instabilities. Low inlet liquid subcoolings result in small-amplitude thermal-fluidic oscillations and the pressure drop instability. Low flow inertia exacerbates the pressure drop instability and results in large-amplitude thermal-fluidic oscillations whereas high flow inertia reduces their severity.

Graphical Abstract
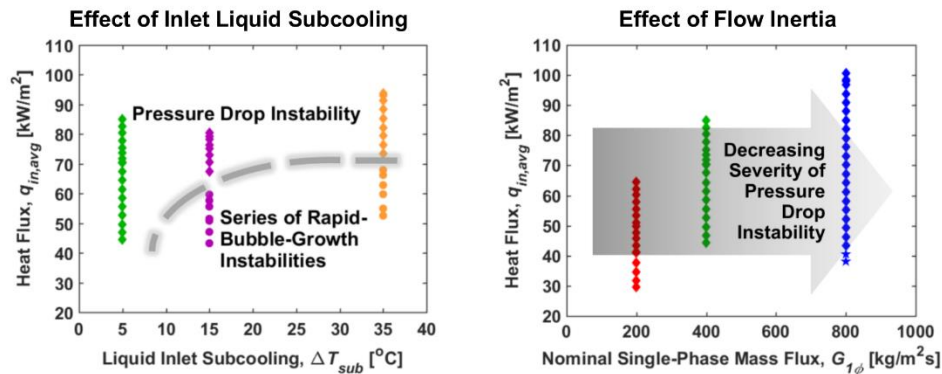
Keywords: dynamic flow boiling instability, microchannel, pressure drop instability, rapid-bubble-growth instability, two-phase flow

Highlights

- Dynamic flow boiling instabilities are studied in a single microchannel.

- Flow instability types and their severity are mapped to operating conditions.

- Low inlet liquid subcooling eliminates the time-periodic rapid-bubble-growth instability.

- Increasing flow inertia reduces the severity of the pressure drop instability.

- Time-periodic thermal-fluidic oscillations are quantitatively characterized.

Nomenclature

D	microchannel inside diameter [μm]
f	characteristic oscillation frequency [Hz]
$\Delta \widetilde{G}_{osc,amp}$	mass flux oscillation amplitude [kg/m^{2}s]
G	mass flux [kg/m^{2}s]
$G_{1\phi}$	nominal single-phase mass flux [kg/m^{2}s]
h	heat transfer coefficient [kW/m^{2}K]
Δp	pressure drop across the microchannel [kPa]
$\Delta \tilde{p}_{osc,amp}$	pressure drop oscillation amplitude [kPa]
p_{in}	inlet pressure [kPa]
p_{out}	outlet pressure [kPa]
p_{sat}	saturation pressure of the fluid [kPa]
P_{in}	power into the microchannel [W]
P_{loss}	power loss to ambient [W]
P_{total}	total power applied [W]
L	microchannel length [m]
L_{heated}	microchannel heated length [m]
t	time [s]
T_{in}	inlet fluid temperature [°C]
$\tilde{T}_{osc,amp}$	wall temperature oscillation amplitude [°C]
T_{out}	outlet fluid temperature [°C]
T_{sat}	saturation temperature of the fluid [°C]
ΔT_{sub}	inlet liquid subcooling relative to outlet saturation temperature [°C]
T_{ref}	reference temperature [°C]

T_{wall}	microchannel outside wall temperature [°C]
$\Delta T_{wall,sup}$	wall superheat relative to reference temperature [°C]
Q	volumetric flow rate [m^3/s]
q_{in}	net heat flux into the microchannel [kW/m^2]
z	axial position of the wall temperature measurement along the heated length of the microchannel [m]

Greek Letters

ρ	liquid density [kg/m^3]

Subscripts

5	5th percentile
95	95th percentile
avg	time-averaged

1 Introduction

Next-generation thermal management strategies capable of dissipating high heat fluxes

will likely need to utilize flow boiling (Agostini *et al.*, 2007). However, designing heat sinks for

two-phase operation and predicting their performance is difficult because of commonly

encountered flow boiling instabilities, which can lead to premature critical heat flux relative to

the conventional dryout mechanism (Bergles and Kandlikar, 2005). Two classes of flow

instabilities have been widely recognized, static and dynamic. Flow is subjected to a static

instability if, when disturbed, its new operating conditions tend asymptotically toward operating

conditions that differ from the initial ones (Kakac and Bon, 2008). Flow is subjected to a

dynamic instability when there is sufficient interaction between the inertia of the flow and the

compressibility of the system, leading to delayed feedback (Kakac and Bon, 2008). Dynamic

flow instabilities commonly encountered in microscale applications include rapid-bubble-growth

instability, pressure drop instability (also known as the upstream compressible volume

instability), and parallel channel instability (Koşar *et al.*, 2006); the former two will be investigated in this study.

The rapid-bubble-growth instability is observed in microscale flow boiling systems because the small characteristic channel sizes confine vapor bubbles formed during boiling. This confinement causes the bubbles to significantly influence the operating characteristics of the system, and can cause pressure fluctuations and flow reversal (Barber *et al.*, 2011); under certain operating conditions, this can lead to large wall temperature excursions at the onset of boiling (Kingston *et al.*, 2018).

The pressure drop instability is attributed to the interaction between the vapor within the heated channel and the compressibility in the flow path upstream of the channel (Qu and Mudawar, 2003b). As the amount of vapor within the channel increases, the flow resistance increases. If a compressible upstream volume is present, the liquid flow rate through the channel will decrease and in turn, cause additional vapor generation within the channel. For a constant system flow rate, this momentary reduction in flow rate is confined to the channel and the increased flow resistance within the channel is accompanied by an increase in the inlet pressure of the channel. Once a critical inlet pressure is reached, liquid is forced through the channel and flushes out most of the vapor, thereby reducing the flow resistance and inlet pressure. This highly transient cyclical process is often time-periodic and is classified as the pressure drop instability. The underlying mechanism responsible for the pressure drop oscillations is the cyclical compression and expansion of the upstream compressible volume and its interaction with the vapor within the channel. The pressure drop instability can cause premature critical heat flux when entry of liquid into the heated channel is delayed and vapor occupies most of the channel for a relatively extended period of time.

Several studies that investigated flow boiling instabilities with parallel microchannel configurations reported coupled effects of multiple instability types (Koşar *et al.*, 2006; Kuo and Peles, 2008, 2009; Qu and Mudawar, 2003b). For example, Qu and Mudawar (2003b) investigated pressure drop oscillations and the parallel channel instability in a microchannel heat sink with 21 parallel channels using water as the working fluid. The addition of a throttling valve upstream of the heat sink suppressed the large-amplitude, periodic pressure drop oscillations which enabled the parallel channel instability to be recognized. The throttling valve stiffens the system and minimizes the effects of upstream compressibility, but increases system pressure drop.

Another approach to isolating individual instability types and identifying their underlying mechanisms is to investigate a single-channel configuration in which individual mechanisms can be more easily observed. However, the results of single-channel flow instability studies cannot be meaningfully extended to behavior in parallel microchannel heat sinks because of differences in the hydrodynamic boundary conditions in the two cases. In a parallel channel configuration, the flow rate through an individual channel can fluctuate and a constant pressure drop boundary condition is more representative. To resemble the hydrodynamic boundary conditions of an individual channel in a parallel-channel system, a constant pressure difference between a pressurized reservoir and the ambient is used in the present study to induce fluid flow through a single heated microchannel. This approach, which appears not to have been exploited in the prior literature, removes the confounding parallel channel instability and enables our study of the rapid-bubble-growth instability and pressure drop instability.

High-frequency (≥ 1000 Hz) thermal-fluidic characterization techniques (*e.g.*, measurement of pressure, mass flux, and temperature) are needed to resolve the transient features

associated with dynamic flow boiling instabilities. These techniques have been successfully used to quantify the transient heat transfer mechanisms that occur during flow boiling processes (Bigham and Moghaddam, 2015; Rao *et al.*, 2014). Zhu *et al.* (2017) used high-frequency (1000 Hz) wall temperature measurements to study the effect of adding hydrophilic micropillars to the bottom surface of square microchannels on the pressure drop instability and the resulting wall temperature variations. At heat fluxes just beyond that needed to cause boiling, large-amplitude wall temperature fluctuations were observed due to transitions between single-phase and two-phase flow. As the heat flux or mass flux was increased, the wall temperature oscillation frequency increased. Higher mass fluxes also mitigated flow reversal. The micropillars promoted capillary-assisted rewetting of the wall and reduced the magnitude of the temperature oscillations compared to a smooth surface, but their influence on the hydrodynamic oscillations and the coupled thermal-fluidic behavior was not investigated.

In Part 1 of this two-part study (Kingston *et al.*, 2018), the rapid-bubble-growth instability at the initial onset of boiling was investigated, and under certain operating conditions, was shown to result in large wall temperature excursions. In Part 2 of this two-part study, high-speed flow visualizations are synchronized to high-frequency pressure drop, mass flux, and wall temperature measurements and are used to characterize the time-periodic dynamic flow boiling instabilities in a single heated microchannel with hydrodynamic boundary conditions that resemble an individual channel in a parallel-channel system. Both the transient and time-averaged behaviors are analyzed to understand the effect of flow inertia, inlet liquid subcooling, and heat flux on the hydrodynamic and thermal oscillations.

2 Summary of Experimental Methods

The custom-built experimental facility used in this work is described in detail in Part 1 (Kingston *et al.*, 2018) of this two-part study; a brief description is provided here. The open-loop facility, schematically illustrated in Figure 1, utilizes a pressure difference between a pressurized reservoir and a reservoir that is open to the ambient to deliver degassed, dielectric HFE-7100 liquid (Novec Engineered Fluid, 3M) to the test section. The liquid flow rate and the test section outlet saturation pressure are adjusted using a pair of needle valves. The liquid volumetric flow rate is measured at 2500 Hz using a liquid flow meter. The liquid is preheated to the desired inlet temperature immediately upstream of the test section, using a constant-temperature circulating bath. The inlet and outlet fluid temperatures are measured immediately upstream and downstream of the test section. The inlet and outlet pressure of the microchannel are measured at 2500 Hz using separate pressure transducers; the pressure drop across the test section is taken as the difference between the inlet and outlet pressure measurements. The measurement uncertainties associated with the instrumentation are provided in Part 1 (Kingston *et al.*, 2018).

The test-section microchannel is mounted horizontally between two polyetheretherketone (PEEK) connectors. The circular cross-section microchannel is made of borosilicate glass with an inside diameter of $D = 500$ μm and a wall thickness of 100 μm. The outside surface of the microchannel is custom-coated with an approximately 100 nm-thick layer of indium tin oxide (ITO). The ITO layer is optically transparent and electrically conductive, enabling visualization of the two-phase flow while subjected to uniform Joule heating. Power is supplied to the ITO coating using an adjustable direct current power supply.
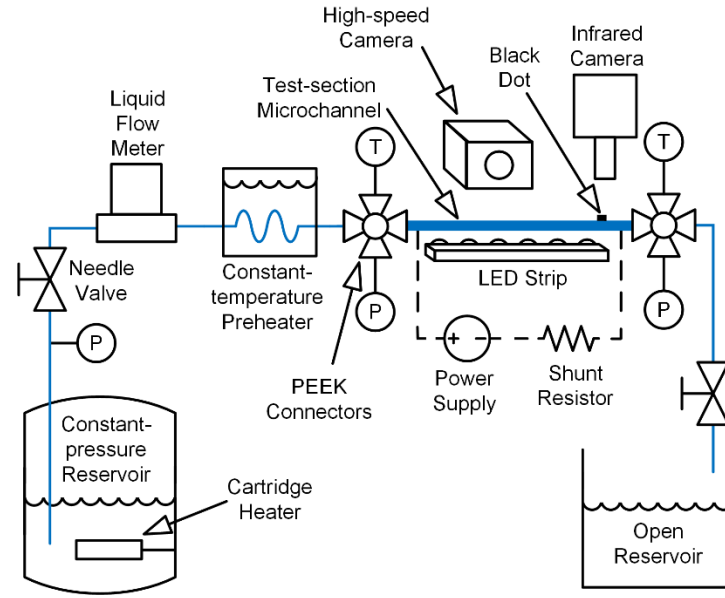
Figure 1. Schematic diagram of the experimental facility featuring a constant pressure reservoir used to deliver fluid flow through the heated test section microchannel.

The microchannel outside wall temperature is measured at a single, fixed location using an infrared (IR) camera at 500 frames per second (fps), which is focused on a single black dot painted on the outside surface of the microchannel. The intensity measured by the IR camera is converted to a temperature using a calibration of the IR camera as detailed in Part 1 of this study (Kingston *et al.*, 2018). The flow through the microchannel is visualized using a high-speed camera at 30,000 fps for a duration of 12 s. An exposure time of 19 μs was used with the high-speed camera to reduce blur. The microchannel is uniformly backlit using a high-intensity light-emitting diode (LED) strip with an integrated light diffuser. High-speed optical and IR images were synchronized to pressure drop, mass flux, and wall temperature measurements using a pulse generator to simultaneously trigger both cameras and the high-frequency DAQ unit.

The test procedure used to capture transient data at the onset of boiling, as described in Part 1 of this study, was extended to investigate the flow instabilities during time-periodic

boiling, after the initial boiling incipience event. Once the desired flow conditions were established, power was applied to the ITO coating on the microchannel in increments, allowing for steady-state conditions to be achieved at each set point. These small increments enable data to be collected over a range of power conditions. At low power conditions, the flow remained a single-phase liquid; synchronized, high-frequency sensor data and IR images were recorded for 6 s once a steady-state condition was achieved. At the minimum power level required to first cause nucleation in the channel, data were recorded to capture this brief boiling onset event that was investigated in Part 1 of this study (Kingston *et al.*, 2018). At all higher power levels, sensor and imaging data were recorded for 12 s once the flow became time-periodic; these results are analyzed in this Part 2 of the study. The increase in power level to the test section continued until the wall temperature was high enough to saturate the IR camera sensor (~ 200 °C).

A portion of the total power supplied to the ITO coating on the microchannel is lost to the ambient. This power loss is a function of the time-averaged wall temperature (over each data acquisition time), resulting in a different power loss for each operating condition; P_{loss} was between 9% - 49% of P_{total}. Details of the procedure used to quantify the power loss to the ambient are provided in Kingston *et al.* (2018). The power into the microchannel is calculated by subtracting the power loss from the total electric power supplied using $P_{in} = P_{total} - P_{loss}$. The time-averaged heat flux into the test section is calculated using $q_{in,avg} = P_{in} / (\pi D L_{heated})$.

The instantaneous mass flux through the test section is calculated using $G = Q\rho / (\pi D^2/4)$ where Q is the measured volumetric flow rate and ρ is the calculated liquid density. The inlet liquid subcooling is determined using $\Delta T_{sub} = T_{sat,out,avg} - T_{in}$ where $T_{sat,out,avg}$ is the time-averaged fluid saturation temperature corresponding to the measured pressure at the outlet of the test section and T_{in} is the inlet fluid temperature. The time-averaged heat transfer coefficient is

calculated using $h_{avg} = q_{in,avg} / (T_{wall,avg} - T_{ref})$, where the reference temperature (T_{ref}) is evaluated

at the location of the wall temperature measurement; in this study, the axial position of the wall

temperature measurement along the heated length of the microchannel is $(z / L_{heated}) = 0.90$. For

single-phase flow, the reference temperature is defined as the liquid temperature at this location

assuming a linear increase in liquid temperature from the inlet to the outlet of the microchannel:

$T_{ref} = T_{in} + (z / L_{heated})(T_{out} - T_{in})$. For two-phase flow, the reference temperature is defined as the

time-averaged local saturation temperature of the two-phase mixture at the location of the wall

temperature measurement, $T_{ref} = T_{sat,avg}$. A time-averaged local saturation pressure is calculated

assuming a linear decrease in the time-averaged pressure from the inlet to the outlet of the

microchannel: $p_{sat,avg} = p_{in,avg} - (z / L_{heated})(p_{in,avg} - p_{out,avg})$. The time-averaged wall superheat is

calculated using $\Delta T_{wall,sup,avg} = T_{wall,avg} - T_{ref}$.

The pressure drop across the test section is calculated as the difference between the test

section inlet and outlet pressures, $\Delta p = p_{in} - p_{out}$. The pressure drop oscillation amplitude is

defined as $\Delta \tilde{p}_{osc,amp} = (\Delta p_{95} - \Delta p_5) / 2)$, where Δp_{95} and Δp_5 are the 95th and 5th percentile of the

pressure drop data recorded over the data acquisition time, respectively; this definition was

chosen because it excludes occasional outlier data. The normalized pressure drop oscillation

amplitude is defined as the ratio of the oscillation amplitude to the time-averaged magnitude

measured over the data acquisition time, $\Delta \tilde{p}_{osc,amp}/\Delta p_{avg}$. This normalized oscillation amplitude

will be used to quantify the pressure drop oscillations. Analogous definitions to those shown

above are used to obtain the normalized mass flux oscillation amplitude, $\tilde{G}_{osc,amp}/G_{avg}$. These

normalized oscillation amplitudes provide a better indication of the relative impact of the

oscillations, making it possible to compare across different operating conditions. A wall

temperature oscillation amplitude, defined as $\tilde{T}_{wall,osc,amp} = (T_{wall,95} - T_{wall,5}) / 2)$, will be used to

quantify the thermal oscillations. These thermal oscillations can be compared across different operating conditions; thus a normalized quantity has not been used.

Five different combinations of nominal single-phase mass flux and inlet liquid subcooling are investigated in this study, as shown in Table 1. The nominal single-phase mass flux is varied, enabling the effect of flow inertia to be studied, while holding the inlet liquid subcooling constant at $\Delta T_{sub} = 5\ °C$. Similarly, the inlet liquid subcooling is varied while holding the nominal single-phase mass flux constant at $G_{1\phi} = 400\ kg/m^2s$. The maximum heat flux applied to the test section differed for each combination of nominal single-phase mass flux and inlet liquid subcooling, as shown in Table 1, due to the sensor saturation criterion of the IR camera used to cease testing.

Table 1. Operating conditions used in this study to investigate dynamic flow boiling instabilities.

Nominal Single-Phase Mass Flux, $G_{1\phi}$ [kg/m²s]	Inlet Liquid Subcooling, ΔT_{sub} [°C]	Heat Flux, $q_{in,avg}$ [kW/m²]
200	5	0 - 64.6
400	5	0 - 85.0
400	15	0 - 80.4
400	35	0 - 93.6
800	5	0 - 100.6

3 Results and Discussion

3.1 Time-Averaged Characteristics

Figure 2 shows the time-averaged wall superheat, heat transfer coefficient, pressure drop, and mass flux as a function of heat flux for the three nominal single-phase mass fluxes at a fixed $\Delta T_{sub} = 5\ °C$. At low heat fluxes, single-phase flow is observed at all mass fluxes (denoted with

open symbols in Figure 2) whereas, at higher heat fluxes, time-periodic boiling is observed (denoted with closed symbols in Figure 2).
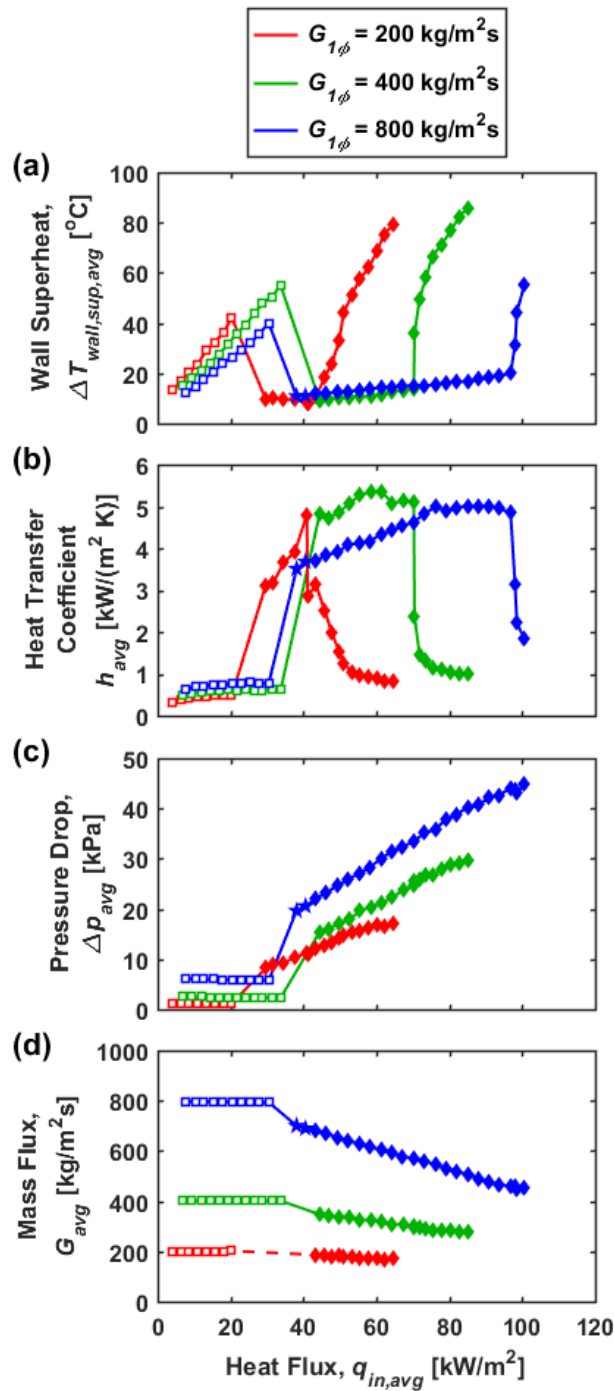

Figure 2. Time-averaged (a) wall superheat, (b) heat transfer coefficient, (c) pressure drop, and (d) mass flux as a function of heat flux for the three nominal single-phase mass fluxes ($G_{1\phi}$ =

200, 400, and 800 kg/m^{2}s) at a fixed inlet liquid subcooling (ΔT_{sub} = 5 °C). Open symbols denote single-phase flow and closed symbols denote time-periodic flow boiling.

The heat transfer trends in the single-phase flow regime are as expected; this regime is characterized by a wall superheat that increases linearly with increasing heat flux (Figure 2a), resulting in a nearly constant heat transfer coefficient (Figure 2b). Once boiling is initiated, the wall superheat reduces significantly, as shown by the sharp downward shift in Figure 2a. This reduction in wall superheat during two-phase flow results from a more efficient heat transfer process compared to single-phase flow, as indicated by the eightfold increase in the heat transfer coefficient at this transition (Figure 2b). Note that the reference temperature used changes between single-phase flow and two-phase flow (as explained in Section 2), but this change has a negligible influence on the aforementioned reduction in wall superheat and increase in the heat transfer coefficient. For all three nominal single-phase mass fluxes tested, there is a minimal change in the wall superheat for a large range of heat fluxes over which boiling occurs (*e.g.*, at $G_{1\phi}$ = 400 kg/m^{2}s, the heat flux increases from 44.4 kW/m^2 to 70.2 kW/m^2, while the wall superheat only increases from 9.2 °C to 13.7 °C). However, at a certain heat flux in each boiling curve (Figure 2a), a transition is observed from a relatively low to a significantly higher wall superheat. Beyond this transitional heat flux, there is also a significant reduction in the heat transfer coefficient as observed in Figure 2b.

The significant increase in wall superheat observed at the transitional heat fluxes (Figure 2a) is attributed to local liquid-vapor interface dynamics at the point of the wall temperature measurement. At these heat fluxes, the liquid film at the wall-temperature measurement location transitions from being wavy and relatively thick at lower heat fluxes to being thin and smooth (*i.e.*, no interfacial waves) for most the data acquisition time. While a thinning liquid film is

14

typically associated with an increasing heat transfer coefficient, this smooth film is observed to correspond to a higher wall superheat, which indicates there is likely intermittent dryout in some locations, resulting in lower heat transfer coefficients. Further investigation of the liquid film behavior at higher-magnification imaging is required to confirm this hypothesis.

In the single-phase regime, the wall superheat at a given heat flux increases with decreasing mass flux (Figure 2a). Additionally, the slope of the wall superheat versus heat flux decreases with increasing mass flux (Figure 2a), indicative of the increased heat transfer coefficient at the higher mass fluxes (Figure 2b) as the hydrodynamic and thermal developing lengths increase. In the boiling regime, the wall superheat at a given heat flux is approximately the same for all three nominal single-phase mass fluxes (Figure 2a) and each case shows comparable heat transfer coefficients (Figure 2b). This indicates that the flow boiling heat transfer performance is relatively independent of flow inertia, as has been observed in microchannels when nucleate boiling heat transfer is the dominant heat transfer mechanism (Harirchian and Garimella, 2008, 2009; Qu and Mudawar, 2003a). However, the transitional heat flux (point above which significant increases in wall superheat occur) is significantly different for the three different nominal single-phase mass fluxes. At $G_{1\phi}$ = 200 kg/m^{2}s, large increases in wall superheat begin at $q_{in,avg}$ = 45.8 kW/m^2 whereas, at $G_{1\phi}$ = 400 kg/m^{2}s and $G_{1\phi}$ = 800 kg/m^{2}s, this behavior is not observed until $q_{in,avg}$ = 70.5 kW/m^2 and $q_{in,avg}$ = 98.0 kW/m^2, respectively. This inertia-dependent behavior has been observed to govern the performance of two-phase heat sinks at higher heat fluxes when nucleate boiling gives way to forced convection boiling as the dominant heat transfer mechanism (Harirchian and Garimella, 2008).

The time-averaged pressure drop across the test section (Figure 2c) can also be correlated to the single-phase and boiling regimes. During single-phase flow, the pressure drop reduces

slightly with increasing heat flux due to a reduction in fluid viscosity with an increase in liquid temperature (Figure 2c); the pressure drop is higher at larger mass fluxes. Once boiling is initiated, the pressure drop increases by factors of 7.1, 6.8, and 3.4 compared to the single-phase flow values, for respective mass fluxes of 200, 400, and 800 kg/m²s, due to vapor generation and the associated accelerational pressure drop. As the heat flux increases, the pressure drop increases linearly through the two-phase regime. The pressure drop is again larger in the two-phase regime at the higher mass fluxes.

Because a constant pressure difference between the pressurized reservoir and the ambient is used to drive the flow, the instantaneous mass flux through the channel can vary with time. While the nominal single-phase mass flux provides a single reference value for each case, Figure 2d shows the time-averaged mass flux as a function of heat flux for the three nominal single-phase mass fluxes. In the single-phase regime, the time-averaged mass flux is nearly constant at its nominal value with increasing heat flux due to a nearly constant pressure drop across the test section. Once boiling occurs, the flow resistance across the test section increases and results in a reduction in the time-averaged mass flux because of the fixed pressure drop across the system (reservoir to ambient). The time-averaged mass flux continues to drop with increasing heat flux throughout the boiling regime. In Figure 2d, for $G_{1\phi}$ = 200 kg/m²s, a dashed line is drawn between the last data point in the single-phase flow regime point and the first data point shown in the two-phase flow regime ($q_{in,avg}$ = 43.5 kW/m²) because for the first six heat fluxes resulting in two-phase flow ($q_{in,avg}$ = 29.7 - 41.2 kW/m²), the mass flux oscillations were so large that they resulted in flow reversal for extended periods of time (as will be shown later in Figure 8 for $q_{in,avg}$ = 37.7 kW/m²). Because the flow meter is unable to measure negative flow rates, the time-

averaged mass flux could not be quantified for these six heat fluxes; hence these points were omitted from the Figure 2d.

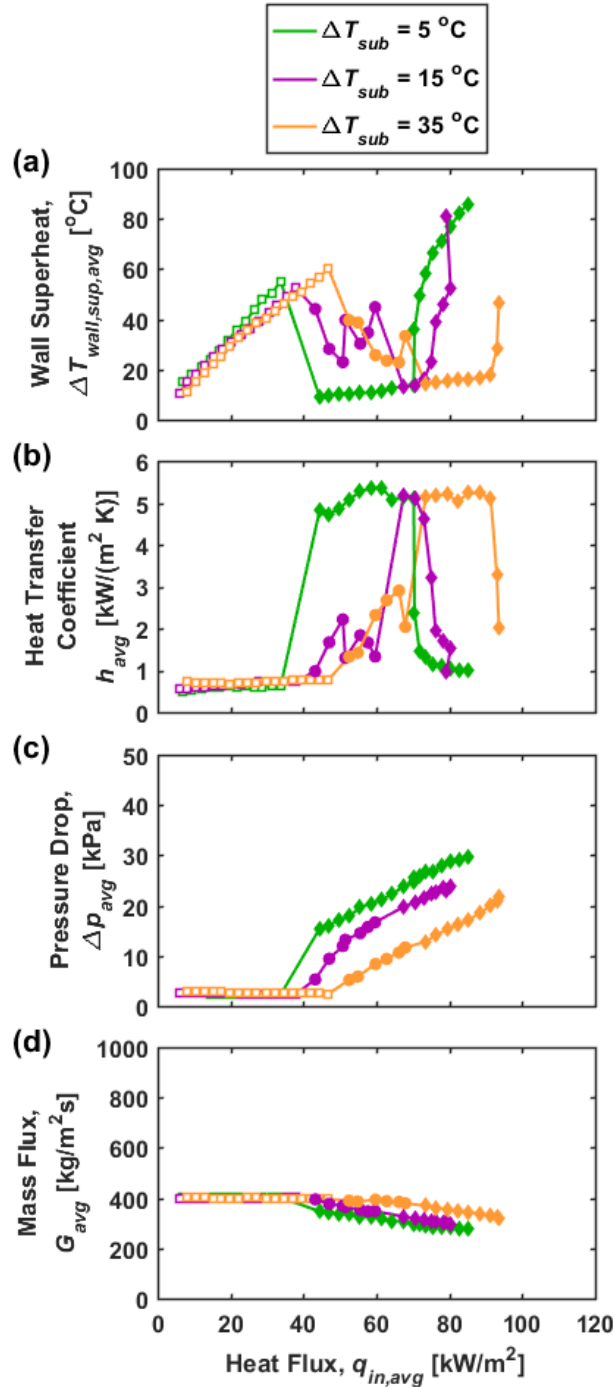Figure 3 shows the time-averaged wall superheat, heat transfer coefficient, pressure drop, and mass flux as a function of heat flux for the three inlet liquid subcoolings at a fixed single-phase mass flux. The case with $\Delta T_{sub} = 5$ °C and $G_{1\phi} = 400$ kg/m²s corresponds to the same case in Figure 2. In the single-phase flow regime, the wall superheat is nearly identical at each heat flux for the three inlet liquid subcoolings (Figure 3a) resulting in nearly identical heat transfer coefficients (Figure 3b). The heat flux required to initiate boiling increases with increasing inlet liquid subcooling because of the larger sensible heating needed. The degree of subcooling and heat flux are shown to significantly affect the time-averaged heat transfer coefficient and wall temperature in the boiling regime. At $\Delta T_{sub} = 5$ °C, the heat transfer coefficient increases eightfold during boiling and is relatively constant until $q_{in,avg} = 70.5$ kW/m², above which it again drops to levels similar to those in the single-phase flow regime. For $\Delta T_{sub} = 15$ °C, the heat transfer coefficient only increases by a factor of 1.4 to 3.1 following boiling incipience, before reaching an eightfold increase at higher heat fluxes within the boiling regime (Figure 3b). Similarly, for $\Delta T_{sub} = 35$ °C, the heat transfer coefficient only increases by factors of 1.7 to 3.7 following boiling incipience, before again reaching the eightfold increase at higher heat fluxes within the boiling regime (Figure 3b). At even higher heat fluxes, the heat transfer coefficient drops significantly and large increases in the wall superheat are observed. The mechanisms causing these variations in the heat transfer coefficient throughout the boiling region will be discussed in Section 3.2.1.

The trends of variation of single-phase pressure drop (Figure 3c) and mass flux (Figure 3d) with heat flux are identical for the three inlet liquid subcoolings. In the boiling regime, the

pressure drop increases linearly with heat flux and is accompanied by a linear reduction in the time-averaged mass flux. For a fixed heat flux in the boiling regime, the pressure drop is the largest for the smallest inlet liquid subcooling because it results in a larger axial length of the microchannel being occupied by two-phase flow. The slope of the pressure drop versus heat flux (Figure 3c) curve as well as that of mass flux versus heat flux (Figure 3d) are approximately equal for the three inlet liquid subcoolings.

Figure 3. Time-averaged (a) wall superheat, (b) heat transfer coefficient, (c) pressure drop, and (d) mass flux as a function of heat flux for three inlet liquid subcoolings (ΔT_{sub} = 5, 15, and 35 °C) at a fixed nominal single-phase mass flux ($G_{1\phi}$ = 400 kg/m²s). Open symbols denote single-phase flow and closed symbols denote time-periodic flow boiling.

3.2 Transient Characterization of Time-Periodic Flow Boiling Instabilities

3.2.1 Effect of Inlet Liquid Subcooling

The type of dynamic instability observed during time-periodic flow boiling is dependent on the operating conditions. Figure 4 maps the two different types of dynamic flow instabilities, *viz*., a time-periodic series of rapid-bubble-growth instabilities and the pressure drop instability, that were observed at different levels of inlet liquid subcooling and heat flux for a fixed $G_{1\phi}$ = 400 kg/m^{2}s. All data points shown in Figure 4 are for time-periodic flow boiling conditions, and correspond to the closed-symbol data points in Figure 3; data points corresponding to single-phase flow have been omitted. For ΔT_{sub} = 15 and 35 °C at low levels of heat flux ($q_{in,avg} \leq 59.7$ kW/m^2 and $q_{in,avg} \leq 67.9$ kW/m^2, respectively), a time-periodic series of rapid-bubble-growth instabilities was observed [denoted with circles in Figure 4]. For the same subcoolings of ΔT_{sub} = 15 and 35 °C at higher levels of heat flux ($q_{in,avg} \geq 67.5$ kW/m^2 and $q_{in,avg} \geq 73.5$ kW/m^2, respectively), as well as for all heat fluxes levels at ΔT_{sub} = 5 °C, the pressure drop instability was observed [denoted with diamond symbols in Figure 4]. Two specific operating conditions (called out in Figure 4) will be described in the following paragraphs to demonstrate the characteristics of these two types of instabilities.
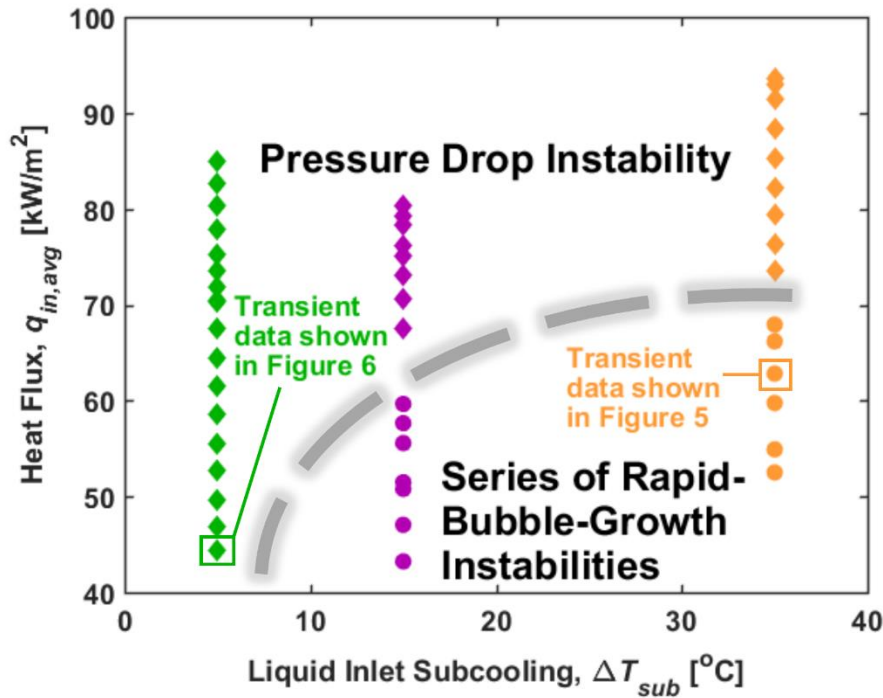
Figure 4. Flow boiling instability types observed at different levels of heat flux and inlet liquid subcooling (for a fixed $G_{1\phi}$ = 400 kg/m²s); the three inlet liquid subcoolings are distinguished by color. Diamond symbols denote flow-boiling operating conditions where the pressure drop instability was observed. Circles denote flow-boiling operating conditions where a time-periodic series of rapid-bubble-growth instabilities was observed. The dashed line demarcates the regions in which each of the two types of flow boiling instabilities are observed.

Figure 5a shows selected images of the two-phase morphology during one cycle of the time-periodic series of rapid-bubble-growth instabilities for $G_{1\phi}$ = 400 kg/m²s, ΔT_{sub} = 35 °C, and $q_{in,avg}$ = 62.8 kW/m² (*i.e.*, orange data point highlighted in Figure 4). Figure 5b shows the synchronized pressure drop, mass flux, and wall temperature for 4 s of the total 12 s of data acquisition time. In Figure 5a, the flow is in the single-phase flow regime at t = 2.373 s; the flow was in a boiling regime immediately prior to this time instant thereby resulting in a relatively low

wall temperature. The wall temperature begins increasing from 78 °C ($t = 2.388$ s) to a

maximum temperature of 109 °C ($t = 2.734$ s) because of the significantly reduced heat transfer

performance associated with single-phase flow compared to two-phase flow; the mass flux and

pressure drop are steady in time. At $t = 2.707$ s, the wall temperature is hot enough that it causes

a small vapor bubble to nucleate from the microchannel wall. The vapor bubble grows very

quickly, in both upstream and downstream directions, until it spans the entire heated length of

the channel (Figure 5a; $t = 2.714$ s). This explosive vapor bubble growth is accompanied by a

spike in the pressure drop, and the mass flux reduces to zero. The latent heat absorbed via

evaporation begins cooling the microchannel wall. When the mass flux increases, it pushes the

upstream portion of the two-phase interface downstream (Figure 5a, 2.726 s $< t <$ 3.190 s).

These observations are identical to those associated with the rapid-bubble-growth instability

described in Part 1 (Kingston *et al.*, 2018) of this two-part study. However, instead of

transitioning into a flow regime with individual bubbles nucleating from the wall [as shown in

Part 1 (Kingston *et al.*, 2018) for $G_{1\phi}$ = 400 kg/m^{2}s and ΔT_{sub} = 5 °C], all the vapor is pushed

out of the heated channel (Figure 5a, $t = 3.233$ s) and the relatively low wall temperature (T_{wall} =

78 °C) begins to increase again. Single-phase flow is observed and the process repeats. The

large-amplitude, low-frequency time-periodic wall temperature oscillations shown in Figure 5b

result from the flow transitioning between single-phase and two-phase flow. Additionally, these

flow transitions result in the previously noted wall superheat and heat transfer coefficient

characteristics shown in Figure 3a and 3b, that yield time-averaged performance somewhere in

between that of single-phase flow and two-phase flow. A large inlet liquid subcooling (ΔT_{sub} =

15 or 35 °C) causes this phenomenon to occur because the cool incoming liquid quenches the

heated microchannel wall and stops the nucleation of vapor bubbles during depressurization of
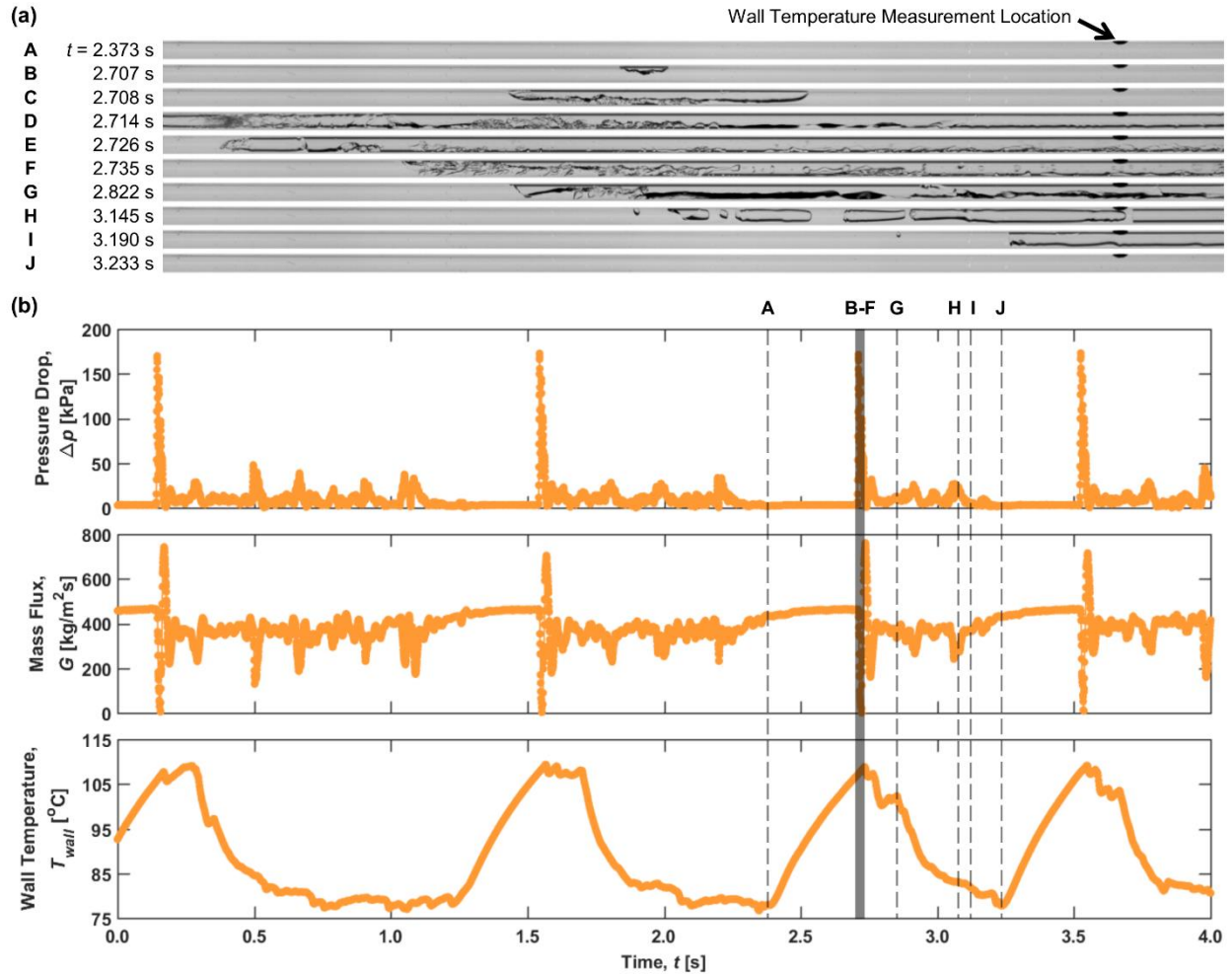
the upstream compressible volume.

Figure 5. (a) Selected images of the time-periodic two-phase morphology for $G_{1\phi}$ = 400 kg/m²s,

ΔT_{sub} = 35 °C, and $q_{in,avg}$ = 62.8 kW/m² (*i.e.*, orange data point highlighted in Figure 4) for one

cycle in a series of time-periodic rapid-bubble-growth instabilities. The entire heated portion of

the microchannel (L_{heated} / D = 84) is shown in (a). (b) Synchronized pressure drop, mass flux,

and wall temperature data. The gray box in (b) correlates to the flow visualizations shown in (a).

A corresponding video of the synchronized flow visualizations and thermal-fluidic signatures is

available online in the Supplementary Materials (Video S1).

As shown in Figure 4, for $q_{in,avg} \geq 67.5$ kW/m^2 at $\Delta T_{sub} = 15$ °C and $q_{in,avg} \geq 73.5$ kW/m^2 for $\Delta T_{sub} = 35$ °C, a time-periodic series of rapid-bubble-growth instabilities is no longer observed because these larger heat fluxes allow vapor bubbles to continue to nucleate during instances of high mass flux quenching; the pressure drop instability is observed. Additionally, for a low inlet liquid subcooling of $\Delta T_{sub} = 5$ °C, the series of rapid-bubble-growth instabilities is not observed for any heat flux level shown in Figure 4 because the incoming liquid is much warmer and does not quench the microchannel wall; the pressure drop instability is observed at this low inlet liquid subcooling.

Figure 6a shows selected images of one cycle of the time-periodic two-phase morphology for $G_{1\phi} = 400$ kg/m^{2}s, $\Delta T_{sub} = 5$ °C, and $q_{in,avg} = 44.4$ kW/m^2 (*i.e.*, green data point highlighted in Figure 4) observed during the pressure drop instability. Figure 6b shows the synchronized pressure drop, mass flux, and wall temperature for 0.5 s of the total 12 s of data acquisition time. At $t = 0.050$ s, small vapor bubbles nucleate and depart from the channel wall and are carried downstream by the relatively high mass flux ($G \approx 400$ kg/m^{2}s). At $t = 0.073$ s, these small vapor bubbles become stagnant and begin to grow circumferentially until they become confined and occupy most of the channel cross-section near the nucleation site, leaving only a thin liquid layer adjacent to the channel wall (Figure 6a; $t = 0.073$ s). The confined vapor bubbles grow in both upstream and downstream directions, rather than being carried downstream after departing from the wall as did the small vapor bubbles. Local flow reversal and increased flow resistance due to additional vapor within the channel increases the pressure drop to 26 kPa at $t = 0.079$ s, decreases the mass flux, and pressurizes the upstream compressible volume. The confined vapor bubbles grow and coalesce until the entire channel is filled with a long continuous vapor bubble (Figure 6a; $t = 0.088$ s). Once the channel is virtually filled with vapor in the annular regime, the

flow resistance decreases and the pressure drop reduces to 10 kPa at $t = 0.103$ s (Figure 6b).

This depressurizes the upstream compressible volume which increases the channel pressure drop

and mass flux, until the furthest upstream portion of the vapor-liquid interface begins to enter the

heated portion of the channel (Figure 6a; $t = 0.123$ s). The reduction in the portion of the

channel length occupied by vapor reduces the flow resistance and causes the pressure drop to

decrease again even as the mass flux continues to increase. The mass flux continues to increase

until it returns to a peak of 413 kg/m^{2}s at $t = 0.149$ s, when the two-phase morphology again

features individual bubbles nucleating and departing from a fixed location on the inside of the

microchannel wall. This cyclical process then repeats. The cyclical oscillations in the wall

temperature can also be correlated to the hydrodynamic oscillations and two-phase morphology.

At each local minimum in the periodic mass flux signal, there is a local maximum in the periodic

wall temperature signal. These time instances correspond to when vapor spans the entire channel

length and resembles an annular flow regime. These characteristic fluctuations in the two-phase

morphology, pressure drop, mass flux, and wall temperature define the pressure drop instability

that occurs because of delayed interaction between the compressible volume upstream of the test

section and the inertia of the flow.

Periodic pressure oscillations caused by flow boiling instabilities have been well-

documented in the literature. However, the parallel channel configurations used in some of these

studies prevents temporal resolution of the relationship between pressure drop and the mass flux

through an individual channel (Chang and Pan, 2007; Qu and Mudawar, 2003b; Wang *et al.*,

2008). Previous studies utilizing a single channel configuration either did not capture high-

frequency mass flux oscillations due to instrumentation limitations (Fan and Hassan, 2012; Huh

et al., 2007; Wang and Cheng, 2008), or used experimental methods that produced a constant

channel mass flux (Barber *et al.*, 2011; Barber *et al.*, 2009). The unique single-channel experimental facility used in this study, which enables the channel mass flux to vary in time, permits the relationship between the time-varying two-phase morphology, pressure drop, mass flux, and wall temperature to be characterized.

For each oscillation period in Figure 6b, there are two peaks in the pressure drop signal for every peak in the mass flux: one larger-magnitude peak due to increased flow resistance from the presence of more vapor within the channel, and a second smaller-magnitude peak due to depressurization of the upstream compressible volume which increases the pressure drop across, and mass flux through, the channel with an approximately constant amount of vapor.
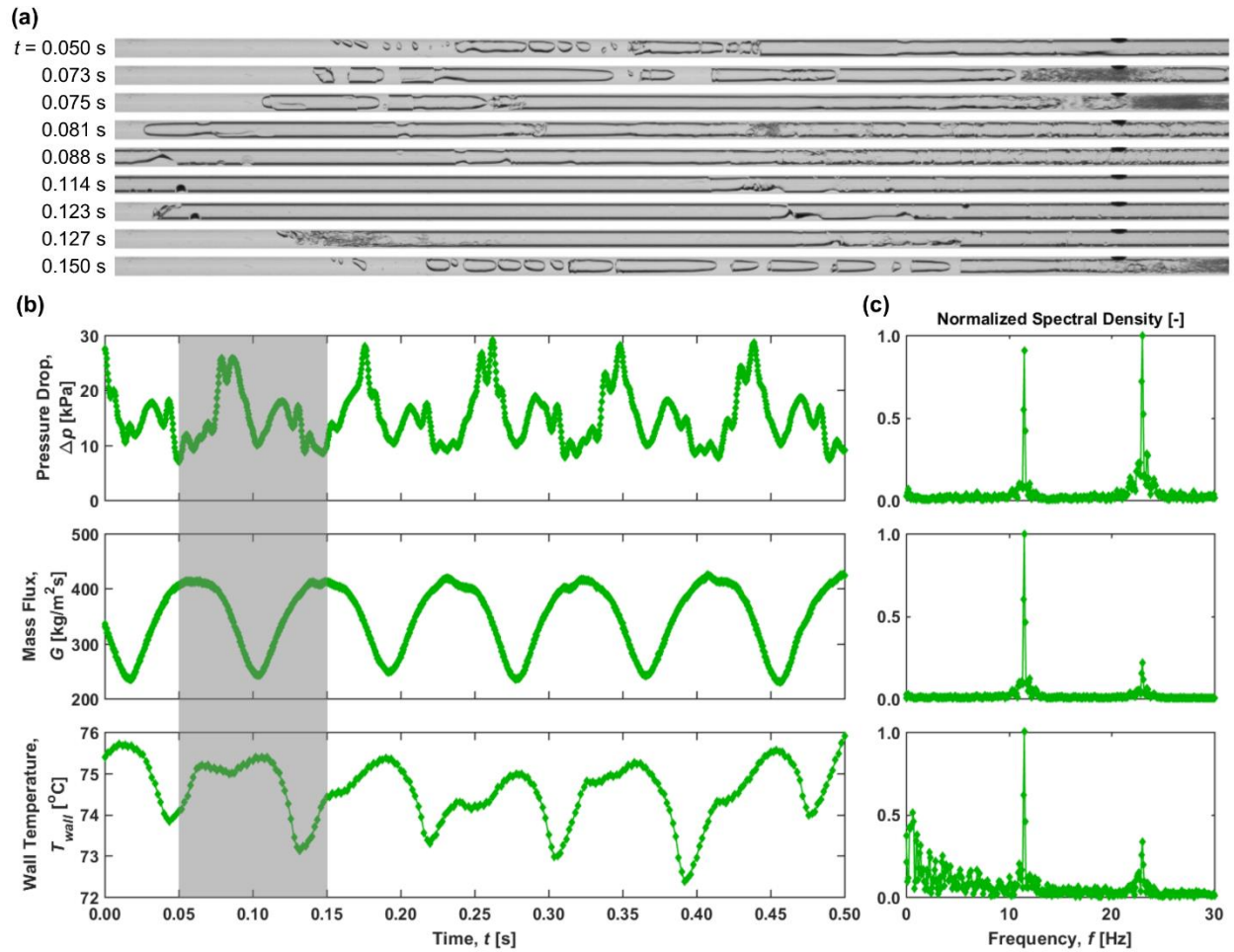
Figure 6. (a) Selected images showing the time-periodic two-phase morphology resulting from the pressure drop instability, (b) synchronized pressure drop, mass flux, and wall temperature fluctuations, and (c) normalized spectral density of the pressure drop, mass flux, and wall temperature data, for $G_{1\phi}$ = 400 kg/m²s, ΔT_{sub} = 5 °C, and $q_{in,avg}$ = 44.4 kW/m². The gray box in (b) correlates to the flow visualizations shown in (a). A corresponding video of the synchronized flow visualizations and thermal-fluidic signatures is available online in the Supplementary Materials (Video S2).

To identify the characteristic frequencies of the time-periodic oscillations, a fast Fourier transform (FFT) is applied to the pressure drop, mass flux, and wall temperature data collected over the 12 s of total data acquisition time in each case. Figure 6c shows the normalized spectral density of these data for frequencies below 30 Hz (where all the spectral density is concentrated). The amplitude of the spectral density resulting from the FFT transformation is normalized relative to the maximum spectral density in each case.

In Figure 6c, two notable frequencies are easily identifiable at 11.5 Hz and 23 Hz. The two frequencies have nearly equal normalized spectral density magnitudes in the pressure drop signal. The flow visualizations (Figure 6a) showed the characteristic oscillation frequency for the pressure drop oscillations to be 11.5 Hz. The frequency of 23 Hz results from a 11.5 Hz fluctuation in pressure drop resulting from increased flow resistance due to accumulation of vapor within the channel and a 11.5 Hz fluctuation in pressure drop resulting from depressurization of the upstream compressible volume which increases the pressure drop and mass flux at an approximately constant void fraction within the channel, which are out of phase by one-half cycle. Thus, for this case, the 11.5 Hz oscillation frequency corresponding to characteristic pressure drop oscillations will be used for further analysis. For the mass flux and wall temperature, the spike in normalized spectral density at 11.5 Hz is significantly more dominant. In the case of the wall temperature, there are also low-magnitude, low-frequency (< ~8 Hz) oscillations that appear. However, these oscillations do not appear to be linked to flow hydrodynamics, given that they do not appear in the pressure drop or mass flux spectra.

For each combination of nominal single-phase mass flux and inlet liquid subcooling shown in Table 1, such spectral analyses were performed at each heat flux that resulted in two-phase flow. From this complete set of spectral data (not shown), a single characteristic

oscillation frequency corresponding to the maximum normalized spectral density for the pressure drop, mass flux, and wall temperature was extracted, which is used as a measure to assess the effect of operating conditions on the oscillation frequency. The effect of inlet liquid subcooling on the hydrodynamic and thermal oscillations during flow-boiling operating conditions is discussed in detail in Appendix A. The level of inlet liquid subcooling is shown to have a dramatic effect on the amplitude and frequency of the hydrodynamic and thermal oscillations during flow boiling due primarily to differences in the type of flow instability that is occurring. Specifically, the wall temperature oscillation amplitude is significantly larger for operating conditions producing a time-periodic series of rapid-bubble-growth instabilities compared to the pressure drop instability.

3.2.2 Effect of Flow Inertia

The severity of the hydrodynamic and thermal oscillations resulting from the pressure drop instability is dependent on the level of flow inertia. For low levels of flow inertia, the oscillations are more severe whereas high levels of flow inertia moderate the amplitude of the oscillations. The pressure drop instability can even be fully suppressed if the flow inertia is high ($G_{1\phi}$ = 800 kg/m^{2}s) and a low heat flux ($q_{in,avg} \leq 40.5$ kW/m^2) is supplied to the heated channel. The qualitative trend of decreasing severity of the pressure drop instability with increasing flow inertia for varying heat fluxes, at the three levels of the nominal single-phase mass flux considered in this study, is depicted pictorially in Figure 7, while a quantitative discussion is provided in the succeeding paragraphs and figures. The data points shown in Figure 7 correspond to the closed-symbol data points in Figure 2, which represent time-periodic flow boiling conditions.
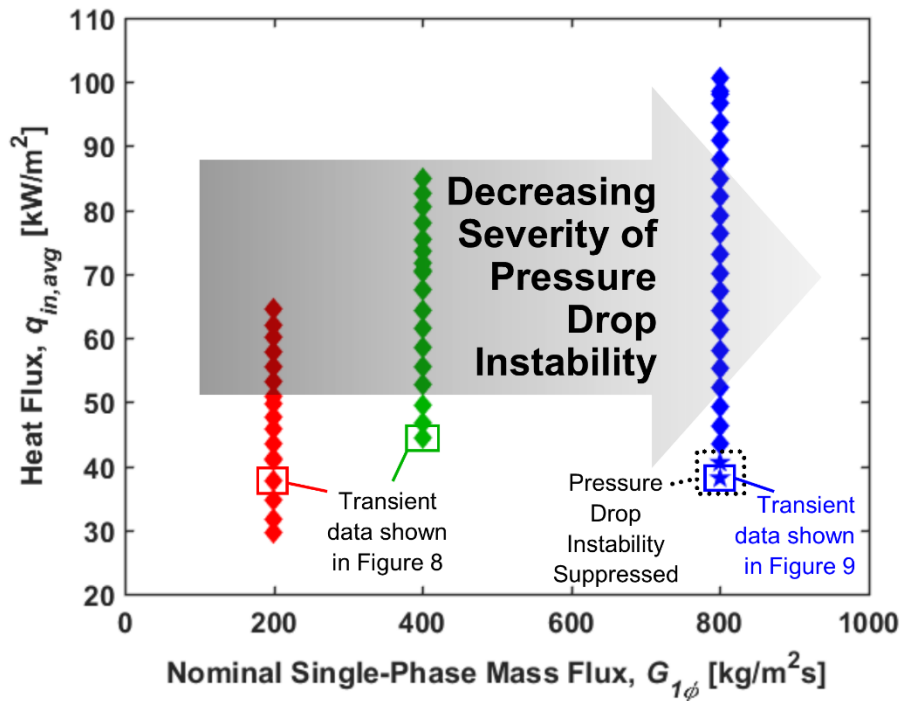
Figure 7. Trend of decreasing severity of the pressure drop instability with increasing flow inertia for the different heat fluxes and nominal single-phase mass fluxes (for a fixed $\Delta T_{sub} = 5$ °C). Diamond symbols denote flow boiling conditions where the pressure drop instability was observed. Star symbols denote flow boiling conditions where the pressure drop instability was suppressed and no other flow instabilities were observed.

The reduction in oscillation severity with increasing flow inertia is quantitatively illustrated in Figure 8 using synchronized pressure drop, mass flux, and wall temperature data for a low flow inertia condition of $G_{1\phi} = 200$ kg/m²s [$\Delta T_{sub} = 5$ °C and $q_{in,avg} = 37.7$ kW/m² (in red)] and an intermediate flow inertia condition of $G_{1\phi} = 400$ kg/m²s [$\Delta T_{sub} = 5$ °C and $q_{in,avg} = 44.4$ kW/m² (in green)] . The pressure drop oscillations shown in Figure 8 for $G_{1\phi} = 200$ and 400 kg/m²s are approximately the same, with a range of approximately 25 kPa. However, for $G_{1\phi} = $

200 kg/m^{2}s, the mass flux oscillations are extreme, ranging from 0 to 938 kg/m^{2}s, whereas for $G_{1\phi}$ = 400 kg/m^{2}s, the mass flux oscillations are much smaller, ranging from 231 to 423 kg/m^{2}s. Recall from Section 3.1 that the flow meter is unable to measure negative flow rates and the signal flatlines to a mass flux of zero when there is flow reversal in the vicinity of the flow meter for $G_{1\phi}$ = 200 kg/m^{2}s. The wall temperature oscillations for $G_{1\phi}$ = 200 kg/m^{2}s are also more severe than for $G_{1\phi}$ = 400 kg/m^{2}s, a direct result of the larger hydrodynamic oscillations associated with $G_{1\phi}$ = 200 kg/m^{2}s. The amplification of the hydrodynamic and thermal oscillations in the case of $G_{1\phi}$ = 200 kg/m^{2}s results from the decreased flow inertia, causing a greater susceptibility to the pressure drop instability, relative to the increased flow inertia case of $G_{1\phi}$ = 400 kg/m^{2}s.
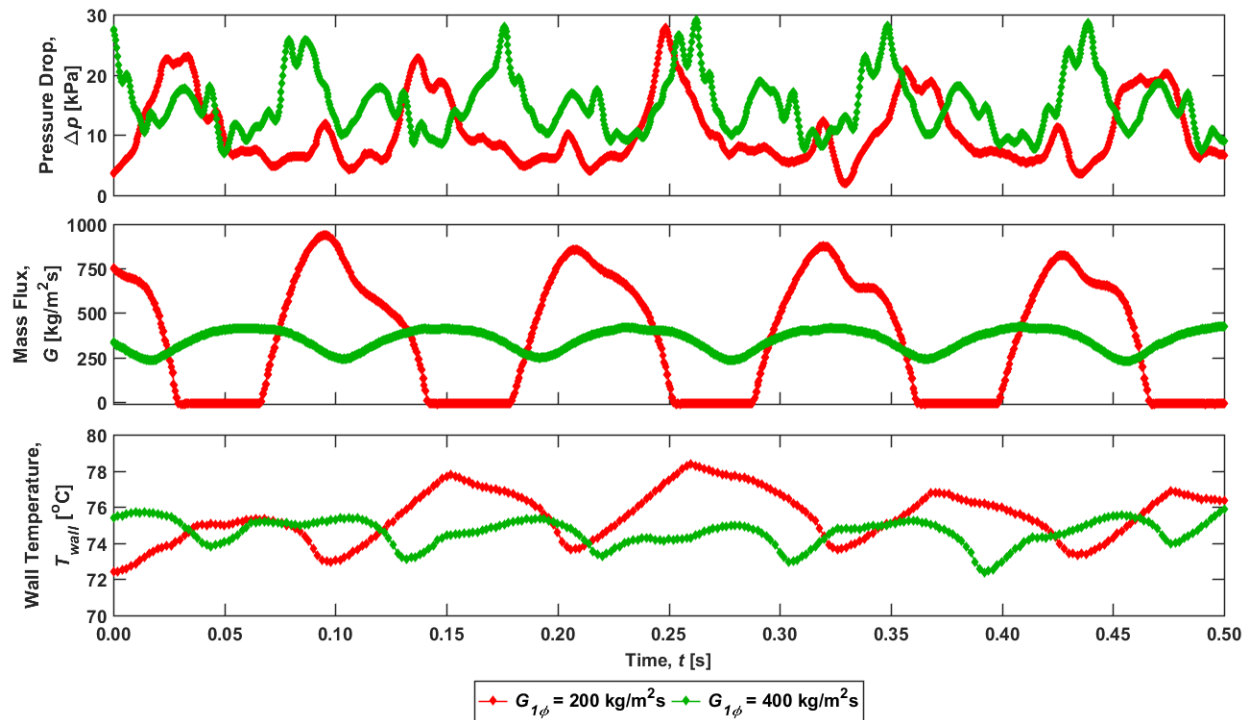
Figure 8. Synchronized pressure drop, mass flux, and wall temperature for $G^{1\phi} = 200$ kg/m²s

[$\Delta T_{sub} = 5$ °C , and $q_{in,avg} = 37.7$ kW/m² (in red)] and for $G_{1\phi} = 400$ kg/m²s [$\Delta T_{sub} = 5$ °C, and

$q_{in,avg} = 44.4$ kW/m² (in green)]. The data for $G_{1\phi} = 400$ kg/m²s are identical to those shown in

Figure 6, but have been replotted to enable a direct comparison to the $G_{1\phi} = 200$ kg/m²s case.

Corresponding videos of the synchronized flow visualizations and thermal-fluidic signatures for

both cases are available online in the Supplementary Materials (Videos S2 and S3).

While a further increase in the flow inertia from $G_{1\phi} = 400$ kg/m²s to $G_{1\phi} = 800$ kg/m²s

did slightly reduce the severity of the pressure drop oscillations further, the effect is much

smaller than the change from $G_{1\phi} = 200$ kg/m²s to $G_{1\phi} = 400$ kg/m²s (data for $G_{1\phi} = 800$

kg/m²s are not included in Figure 8). However, for the two lowest heat flux levels of $q_{in,avg} =$

38.1 kW/m² and 40.5 kW/m², the pressure drop instability was completely suppressed at $G_{1\phi} =$

800 kg/m². Figure 9a shows selected images in 0.002 s increments illustrating one periodic cycle

that depicts the nucleation, departure, and growth of a single vapor bubble that occurs repeatedly

during this operating condition. The vapor bubble nucleates, departs almost immediately, and

grows as it flows downstream. Local flow reversal and pressurization of the upstream

compressible volume are not observed, thus eliminating the pressure drop instability. Figure 9b

shows the synchronized pressure drop, mass flux, and wall temperature for a 0.5 s period

extracted from the 12 s data acquisition time; this behavior was observed throughout the entire

recording. Owing to suppression of the pressure drop instability, the pressure drop, mass flux,

and wall temperature oscillation amplitudes are much lower compared to those shown in Figure

8. The elimination of the pressure drop instability, in this case, is a result of the relatively

increased flow inertia compared to the upstream compressibility. At $q_{in,avg} \geq 43.4$ kW/m^2, the

time-averaged mass flux (and thus, flow inertia) decreases (as shown in Figure 2) and results in

more vapor within the channel, causing compressibility to become dominant. This leads to a

transition to a flow regime featuring the pressure drop instability, like that shown in Figure 6. It

is expected that at even higher nominal single-phase mass fluxes, the pressure drop instability

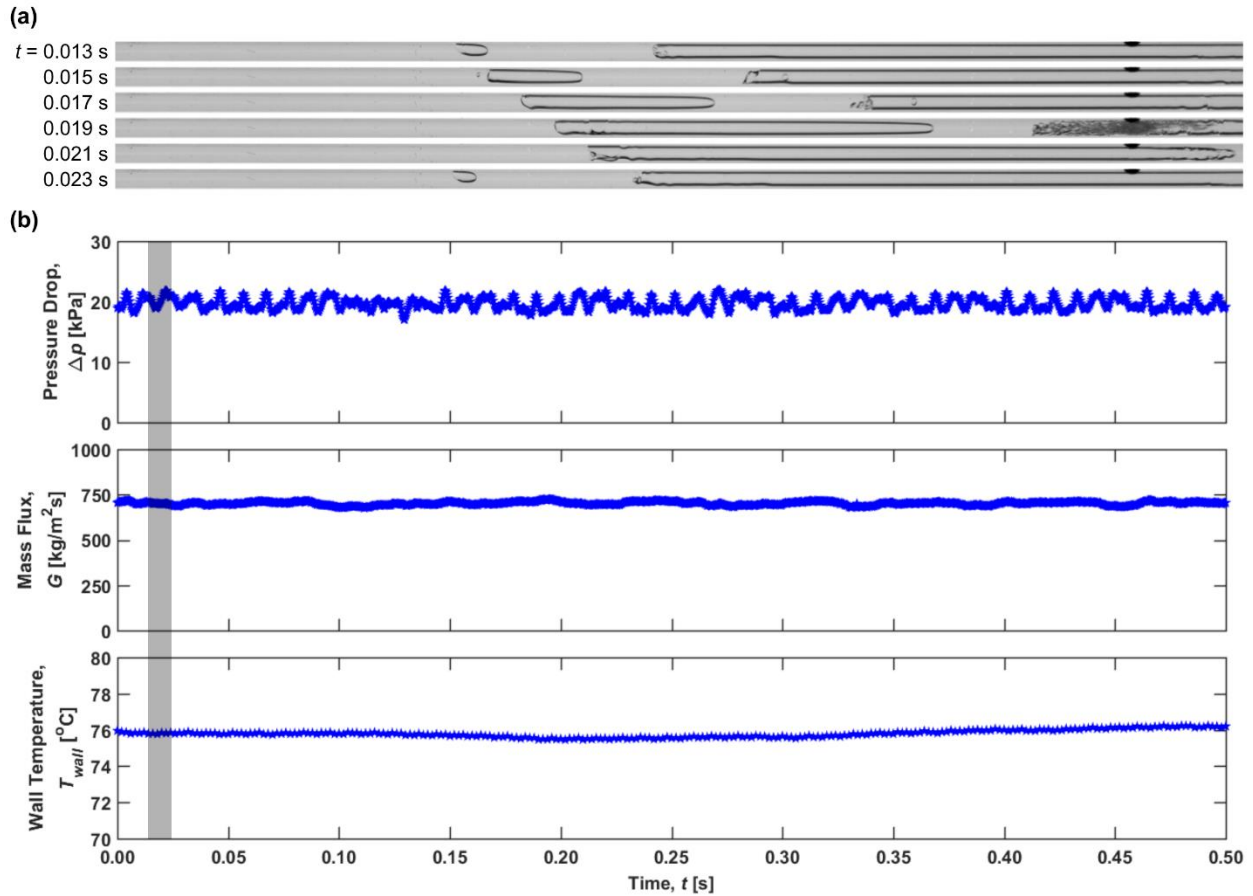would be suppressed even at larger heat fluxes.

Figure 9. (a) Selected images showing the periodic nucleation, departure, and growth of a vapor

bubble, and (b) synchronized pressure drop, mass flux, and wall temperature for $G_{1\phi} = 800$

kg/m^{2}s, $\Delta T_{sub} = 5$ °C, and $q_{in,avg} = 38.1$ kW/m^2. Data are plotted on identical axes to those in

Figure 8 to enable quantitative comparison. A corresponding video of the synchronized flow

33

visualizations and thermal-fluidic signatures is available online in the Supplementary Materials (Video S4).

The level of flow inertia significantly affects the amplitude of the hydrodynamic oscillations during flow-boiling operating conditions. Specifically, low levels of flow inertia result in large hydrodynamic oscillations because the ratio of flow inertia to upstream compressibility is smaller. A complete discussion of the effect of flow inertia on the hydrodynamic and thermal oscillation amplitudes and their characteristics frequencies during flow-boiling operating conditions is provided in Appendix B.

4 Conclusions

A constant pressure source was used to deliver fluid flow through a single microchannel subjected to a uniform heat flux while synchronized high-speed flow visualizations and high-frequency pressure, mass flux, and temperature measurements were acquired. The effect of flow inertia, inlet liquid subcooling, and heat flux on the time-averaged hydrodynamic and heat transfer performance and the dynamic rapid-bubble-growth and pressure drop instabilities are reported in Part 2 of this two-part study. Two different types of dynamic instabilities are observed: (a) time-periodic transitions between single-phase and two-phase flow, which lead to a time-periodic series of rapid-bubble-growth instabilities, resulting in flow reversal and large increases in wall temperature, and (b) the pressure drop instability resulting in time-periodic pressure drop, mass flux, and wall temperature oscillations. The characteristic frequencies of the oscillations are quantified using spectral analysis. The parametric study enabled the following key conclusions to be drawn regarding the effect of operating conditions on the dynamic flow boiling instabilities:

Effect of inlet liquid subcooling at a constant nominal single-phase mass flux ($G_{1\phi}= 400$

kg/m^{2}s):

- High levels of inlet liquid subcooling (*i.e.*, $\Delta T_{sub} = 15$ and 35 °C) and low heat fluxes produce a time-periodic series of rapid-bubble-growth instabilities, resulting in large-amplitude, low-frequency wall temperature oscillations.

- The pressure drop instability is observed for (i) high levels of inlet liquid subcooling when subjected to high heat fluxes, and (ii) low levels of inlet liquid subcooling (*i.e.*, $\Delta T_{sub} = 5$ °C) independent of the heat flux.

Effect of flow inertia at a constant inlet subcooling ($\Delta T_{sub} = 5$ °C):

- Low levels of flow inertia exacerbate the pressure drop instability and result in more severe hydrodynamic and thermal oscillations.

- Higher flow inertia reduces the hydrodynamic and thermal oscillations associated with the pressure drop instability, and in the cases with high flow inertia ($G_{1\phi}= 800$ kg/m^{2}s) and low heat fluxes ($q_{in,avg} \leq 40.5$ kW/m^2), completely suppresses the pressure drop instability.

Appendix A

The normalized pressure drop oscillation amplitude ($\Delta\tilde{p}_{osc,amp}/\Delta p_{avg}$), mass flux oscillation amplitude ($\Delta\tilde{G}_{osc,amp}/\Delta G_{avg}$), wall temperature oscillation amplitude ($\tilde{T}_{wall,osc,amp}$), and their corresponding oscillation frequency(f) (defined in Sections 2 and 3.2.2) in the measured thermal-fluidic signatures for the three inlet liquid subcoolings and all heat fluxes resulting in two-phase flow are shown in Figure A1 for a fixed $G_{1\phi}$ = 400 kg/m²s. Data points corresponding to single-phase flow are omitted because the oscillation amplitudes are negligible and oscillation frequencies are random.

The most significant effects are in the wall temperature oscillation amplitude (Figure A1c). At $q_{in,avg} \leq 59.7$ kW/m² for ΔT_{sub} = 15 °C (purple circles in Figure A1c), the wall temperature oscillation amplitude ($\tilde{T}_{wall,osc,amp}$) is significantly larger (19-54 °C), due to the time-periodic series of rapid-bubble-growth instabilities. At $q_{in,avg} \geq 67.5$ kW/m², the wall temperature oscillation amplitude is less than 3 °C (similar to cases for ΔT_{sub} = 5 °C) because the instability type changes to the pressure drop instability. Similarly, for $q_{in,avg} \leq 67.9$ kW/m² at ΔT_{sub} = 35 °C (orange circles in Figure A1c), the wall temperature oscillation amplitude is significantly larger (16-55 °C). At $q_{in,avg} \geq 73.5$ kW/m², the wall temperature oscillation amplitude reduces to less than 4 °C because, again, the instability type changes to the pressure drop instability.

The wall temperature oscillation frequency (Figure A1f) exactly matches that of the hydrodynamic oscillations frequencies for $q_{in,avg} \leq 55.5$ kW/m² (corresponding to $f \leq 13$ Hz), above which the thermal capacitance of the wall likely damps the thermal oscillations resulting in low-frequency oscillations ($f < 2$ Hz).

The normalized pressure drop oscillation amplitude (Figure A1a) is significantly larger for ΔT_{sub} = 15 °C and 35 °C, relative to ΔT_{sub} = 5 °C. These large values for ΔT_{sub} = 15 °C and 35 °C stem from (i) larger pressure drop oscillation amplitudes, and (ii) lower time-averaged pressure drops (as shown in Figure 3c) because of the lower flow resistance resulting from a shorter length of the channel being occupied by vapor in these cases (as more sensible heating is needed to bring the liquid to the saturation temperature) thereby reducing the flow resistance. For all inlet liquid subcoolings, the normalized pressure drop oscillation amplitude decreases slowly with increasing heat flux. The corresponding pressure drop oscillation frequency (Figure A1d) is much smaller for ΔT_{sub} = 15 °C and 35 °C than ΔT_{sub} = 5 °C, particularly at low heat fluxes where the time-periodic series of rapid-bubble-growth instabilities is observed (circles in Figure A1).

For all inlet liquid subcoolings, the pressure drop oscillation frequency increases with increasing heat flux, with a jump from very low-frequency oscillations to higher-frequency oscillations when the instability changes from a time-periodic series of rapid-bubble-growth instabilities to the pressure drop instability for ΔT_{sub} = 15 °C and 35 °C.

Despite differences in the pressure drop oscillation characteristics, the normalized mass flux oscillation amplitudes (Figure A1b) are similar for all three inlet liquid subcoolings. All three cases show a slight increase in normalized oscillation amplitude with increasing heat flux because of a continual increase in the mass flux oscillation amplitude and a continual decrease in the time-average mass flux (as shown in Figure 3d).

The characteristic frequencies of the mass flux oscillations (Figure A1e) are nearly identical to those of the pressure drop (Figure A1d), and are significantly lower for the larger ΔT_{sub} = 15 °C and 35 °C than at ΔT_{sub} = 5 °C. The time-averaged increase in void fraction within

the channel for $\Delta T_{sub} = 5\ °C$ relative to $\Delta T_{sub} = 15\ °C$ and $35\ °C$ likely causes the increase in the

hydrodynamic (pressure drop and mass flux) oscillation frequency when the pressure drop
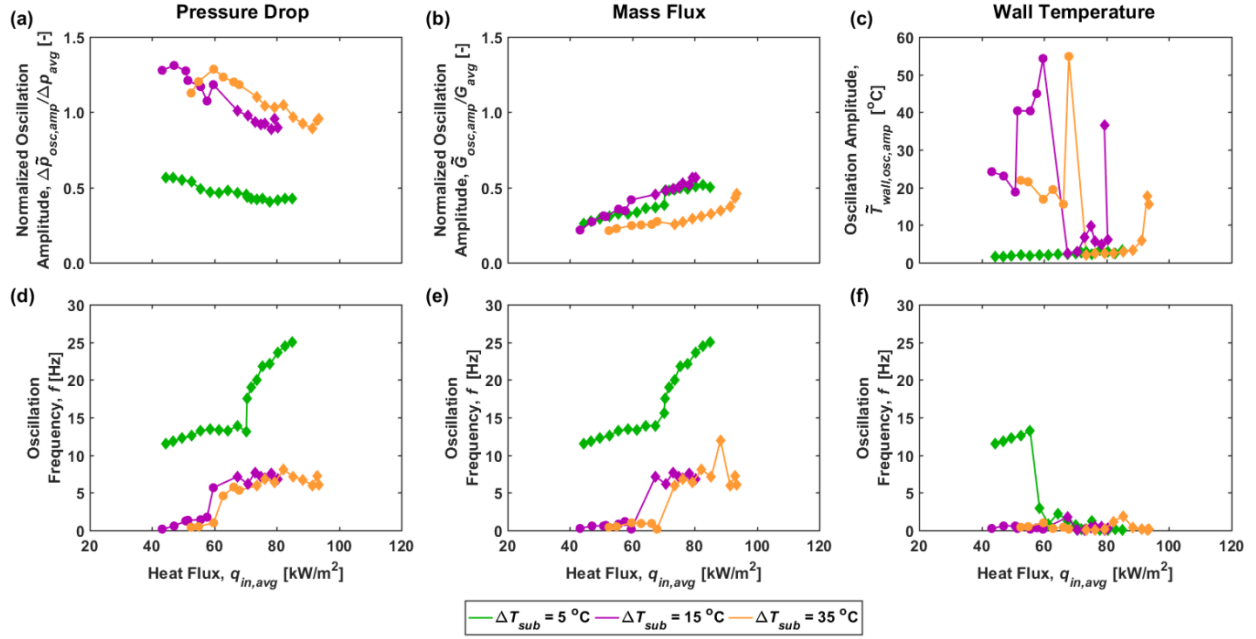
instability is observed.

Figure A1. The (a) normalized pressure drop oscillation amplitude, (b) normalized mass flux

oscillation amplitude, (c) thermal oscillation amplitude, and (d-f) characteristic oscillation

frequency in the measured signals of pressure drop, mass flux, and wall temperature, are shown

as a function of heat flux for $\Delta T_{sub} = 5, 15,$ and $35\ °C$ at a fixed $G_{1\phi} = 400\ kg/m^2s$. Diamond

symbols denote flow-boiling operating conditions where the pressure drop instability was

observed. Circles denote flow-boiling operating conditions where a time-periodic series of

rapid-bubble-growth instabilities was observed.

Appendix B

      The level of flow inertia significantly affects the amplitude of the hydrodynamic

oscillations but has less effect on the thermal oscillations during flow boiling. The normalized

pressure drop oscillation amplitude ($\Delta\tilde{p}_{osc,amp}/\Delta p_{avg}$), mass flux oscillation amplitude ($\Delta\tilde{G}_{osc,amp}/\Delta G_{avg}$), wall temperature oscillation amplitude ($\tilde{T}_{wall,osc}$), and their corresponding characteristic oscillation frequency (f) (defined in Sections 2 and 3.2.2) in the measured thermal-fluidic signatures are shown in Figure B1 at the three nominal single-phase mass fluxes and all heat fluxes resulting in two-phase flow for a fixed $\Delta T_{sub} = 5$ °C. Figure B1a - B1c and the insets in Figure B1d - B1f are plotted on the same axes as Figure A1 to enable a quantitative comparison of the oscillation amplitude and frequencies. Data corresponding to single-phase flow are again omitted as before.

The lowest level of flow inertia (*i.e.*, $G_{1\phi} = 200$ kg/m²s) exacerbates the pressure drop instability and results in large normalized pressure drop and mass flux oscillation amplitudes for all heat flux levels (as shown in Figure B1a and B1b), compared to $G_{1\phi} = 400$ and 800 kg/m²s. The wall temperature oscillations are also slightly larger for all heat flux levels for $G_{1\phi} = 200$ kg/m²s, compared to $G_{1\phi} = 400$ and 800 kg/m²s, particularly for $q_{in,avg} = 41.2 - 51.0$ kW/m²; additional discussion and the transient thermal-fluidic signatures for these heat flux levels are available online in the Supplementary Materials.

The pressure drop (Figure B1d) and mass flux (Figure B1e) characteristic oscillation frequencies are identical to each other for all operating conditions featuring the pressure drop instability (diamond symbols in Figure B1). A gradual increase in the hydrodynamic characteristic oscillation frequency with increasing heat flux is observed for $G_{1\phi} = 200$ and 400 kg/m²s. The wall temperature oscillation frequency (Figure B1f) increases with increasing heat flux for $G_{1\phi} = 200$ and 400 kg/m²s and exactly matches the hydrodynamic oscillation frequencies for $q_{in,avg} \leq 37.7$ kW/m² and $q_{in,avg} \leq 55.5$ kW/m² (corresponding to $f \leq 9$ and 13 Hz,

respectively). Above these heat flux levels, the characteristic wall temperature oscillation frequency switches to lower frequencies, likely due to damping by the thermal capacitance of the wall.

The two lowest heat fluxes at $G_{1\phi} = 800$ kg/m²s that yield two-phase flow ($q_{in,avg} = 38.1$ kW/m² and 40.5 kW/m²) have significantly lower pressure drop and mass flux oscillation amplitudes (Figure B1a and B1b) compared to all other operating conditions. Additionally, their pressure drop characteristic frequencies are extremely high (142.1 Hz and 126.2 Hz, respectively), while the mass flux oscillation frequencies are extremely low (essentially zero). This behavior is due to the suppression of the pressure drop instability (as shown in Figure 9a) at high levels of flow inertia and low heat fluxes.
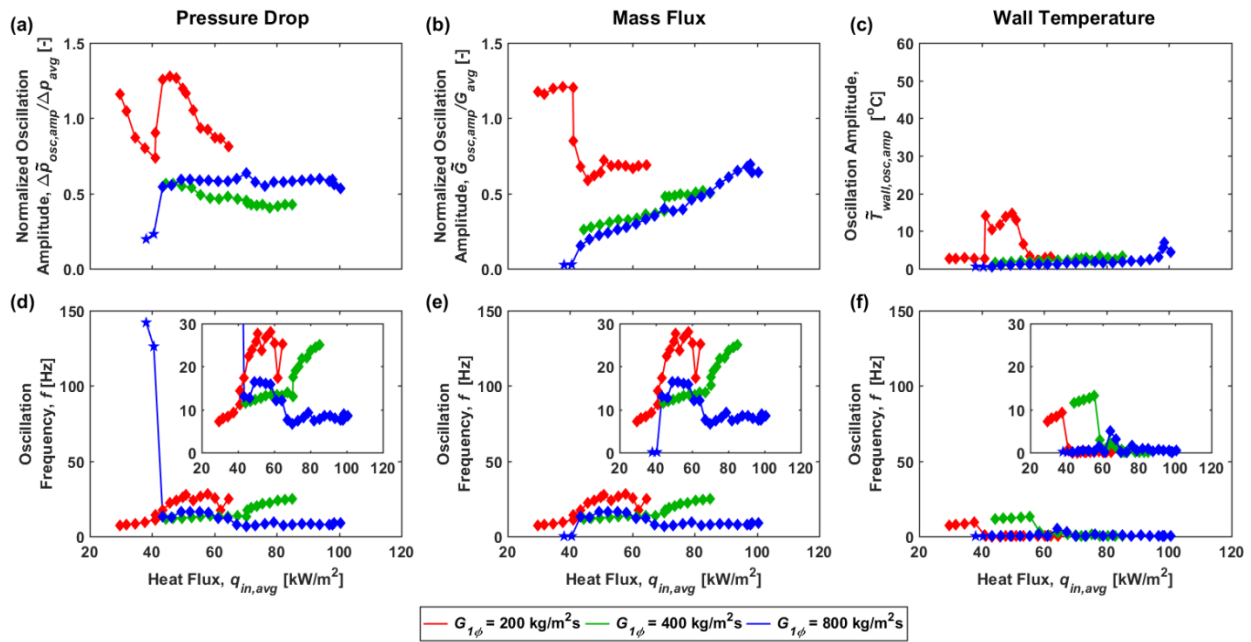

Figure B1. The (a) normalized pressure drop oscillation amplitude, (b) normalized mass flux oscillation amplitude, (c) thermal oscillation amplitude, and (d-f) characteristic oscillation frequency in the measured signals of pressure drop, mass flux, and wall temperature, are shown as a function of heat flux for $G_{1\phi} = 200$, 400, and 800 kg/m²s at a fixed $\Delta T_{sub} = 5$ °C. Diamond

symbols denote flow-boiling operating conditions where the pressure drop instability was observed. Star symbols denote flow-boiling operating conditions where the pressure drop instability was suppressed and no other flow instabilities were observed.

Supplementary Material

Supplementary material associated with this article can be found in the online version.

References

Agostini, B., Fabbri, M., Park, J.E., Wojtan, L., Thome, J.R., Michel, B., 2007. State of the art of high heat flux cooling technologies. Heat Transfer Engineering, 28, 258-281.

Barber, J., Brutin, D., Sefiane, K., Gardarein, J.L., Tadrist, L., 2011. Unsteady-state fluctuations analysis during bubble growth in a "rectangular" microchannel. International Journal of Heat and Mass Transfer, 54, 4784-4795.

Barber, J., Sefiane, K., Brutin, D., Tadrist, L., 2009. Hydrodynamics and heat transfer during flow boiling instabilities in a single microchannel. Applied Thermal Engineering, 29, 1299-1308.

Bergles, A.E., Kandlikar, S.G., 2005. On the nature of critical heat flux in microchannels. Journal of Heat Transfer, 127, 101-107.

Bigham, S., Moghaddam, S., 2015. Microscale study of mechanisms of heat transfer during flow boiling in a microchannel. International Journal of Heat and Mass Transfer, 88, 111-121.

Chang, K.H., Pan, C., 2007. Two-phase flow instability for boiling in a microchannel heat sink. International Journal of Heat and Mass Transfer, 50, 2078-2088.

Fan, Y., Hassan, I., 2012. Experimental Investigation of Flow Boiling Instability in a Single Horizontal Microtube With and Without Inlet Restriction. Journal of Heat Transfer, 134, 081501.

Harirchian, T., Garimella, S.V., 2008. Microchannel size effects on local flow boiling heat transfer to a dielectric fluid. International Journal of Heat and Mass Transfer, 51, 3724-3735.

Harirchian, T., Garimella, S.V., 2009. Effects of channel dimension, heat flux, and mass flux on flow boiling regimes in microchannels. International Journal of Multiphase Flow, 35, 349-362.

Huh, C., Kim, J., Kim, M.H., 2007. Flow pattern transition instability during flow boiling in a single microchannel. International Journal of Heat and Mass Transfer, 50, 1049-1060.

Kakac, S., Bon, B., 2008. A review of two-phase flow dynamic instabilities in tube boiling systems. International Journal of Heat and Mass Transfer, 51, 399-433.

Kingston, T.A., Weibel, J.A., Garimella, S.V., 2018. High-frequency thermal-fluidic characterization of dynamic microchannel flow boiling instabilities: Part 1 - Rapid-bubble-growth instability at the onset of boiling. International Journal of Multiphase Flow (in review).

Koşar, A., Kuo, C.J., Peles, Y., 2006. Suppression of boiling flow oscillations in parallel microchannels by inlet restrictors. Journal of Heat Transfer, 128, 251-260.

Kuo, C.J., Peles, Y., 2008. Flow boiling instabilities in microchannels and means for mitigation by reentrant cavities. Journal of Heat Transfer, 130, 072402.

Kuo, C.J., Peles, Y., 2009. Pressure effects on flow boiling instabilities in parallel microchannels. International Journal of Heat and Mass Transfer, 52, 271-280.

Qu, W., Mudawar, I., 2003a. Flow boiling heat transfer in two-phase micro-channel heat sinks - I. Experimental investigation and assessment of correlation methods. International Journal of Heat and Mass Transfer, 46, 2755-2771.

Qu, W., Mudawar, I., 2003b. Measurement and prediction of pressure drop in two-phase micro-channel heat sinks. International Journal of Heat and Mass Transfer, 46, 2737-2753.

Rao, S.R., Houshmand, F., Peles, Y., 2014. Transient flow boiling heat-transfer measurements in microdomains. International Journal of Heat and Mass Transfer, 76, 317-329.

Wang, G., Cheng, P., 2008. An experimental study of flow boiling instability in a single microchannel. International Communications in Heat and Mass Transfer, 35, 1229-1234.

Wang, G., Cheng, P., Bergles, A.E., 2008. Effects of inlet/outlet configurations on flow boiling instability in parallel microchannels. International Journal of Heat and Mass Transfer, 51, 2267-2281.

Zhu, Y., Antao, D.S., Bian, D.W., Rao, S.R., Sircar, J.D., Zhang, T., Wang, E.N., 2017. Suppressing high-frequency temperature oscillations in microchannels with surface structures. Applied Physics Letters, 110, 033501.